MXene-induced nonradiative energy transfer

Carmen Lorena Manzanares[a], Dahnan Spurling[b], Alan M. Szalai[a,c], Tim Schröder[a], Valeria Nicolosi[b], Philip Tinnefeld[a]**

C. L. Manzanares, A. M. Szalai, T. Schröder, P. Tinnefeld
Department of Chemistry and Center for NanoScience, Ludwig-Maximilians-University, Butenandtstraße 5-13, 81377, Munich, Germany
E-mail: c.manzanares@lmu.de, philip.tinnefeld@cup.lmu.de

A. M. Szalai
CONICET Centro de Investigaciones en Bionanociencias (CIBION), Polo Científico Tecnológico Godoy Cruz 2390, Buenos Aires, Argentina

D. Spurling, V. Nicolosi
School of Chemistry, Trinity College Dublin, Dublin 2, Ireland

Keywords: MXene, DNA origami, energy transfer, single-molecule, fluorescence microscopy, 2D materials

Since their discovery in 2011, MXenes have risen to prominence for energy storage, electromagnetic shielding, and optoelectronics. Yet, the nonradiative energy transfer properties of this family of 2D materials remain elusive, which may have implications in optoelectronics, photovoltaics and biosensing. Here, we use single-molecule fluorescence confocal microscopy and DNA origami nanopositioners to investigate, for the first time, the distance-dependent energy transfer of an organic emitter (ATTO 542) placed on transparent thin films made of spincast $Ti_3C_2T_x$ flakes. We propose a specific immobilization chemistry for DNA origami nanostructures based on glycine-MXene interaction, allowing us to precisely control their orientation on the surface. Each DNA origami structure is designed to carry a single dye molecule at predetermined heights. Our findings reveal that when the dye is located at distances of 1 nm < d < 8 nm from the surface, the fluorescence is quenched following a distance dependence of d^{-3}. This is in agreement with the Förster-type mechanism of energy transfer in transparent conductors at the bulk level. 50% of energy transfer efficiency is reached at 2.7 nm (d_0). MXenes could therefore be used as short-distance

spectroscopic nanorulers, sensitive at a distance regime that common energy transfer tools cannot access.

1. Introduction

The phenomenon of non-radiative energy transfer (ET) from a donor to an acceptor system has been well-understood for decades.[1–3] The process is strongly distance-dependent following a near field interaction and its efficiency is contingent on several factors, including spectral overlap between the donor's emission and the acceptor's absorption, screening of the electric field of the donor transition-dipole-moment (TDP) in the surrounding medium, and the dimensionality of the donor and acceptor.

A well-known example of distance-dependent non-radiative energy transfer is Förster resonance energy transfer or FRET,[3] where a donor dye in the excited state transfers its energy to an acceptor dye in the ground state. Biomolecules are labeled with a donor-acceptor pair and the d^{-6} distance dependence of the energy transfer between the two in the 3-10 nm range is typically used to monitor conformational changes, dynamics, and binding. While the technique has served as a spectroscopic nanoruler for decades, measuring absolute distances with it remains challenging. This complexity arises from various factors such as the nontrivial dependencies on the relative orientations of donor and acceptor molecules, which render the analysis and interpretation of FRET data an intricate task.[4–8]

In surface-induced ET, only one dye label (donor) is required and substrates like metal films and graphene act as dark, broadband and unbleachable energy acceptors, eliminating issues such as bleed-through of donor emission, direct acceptor excitation, and problems arising from acceptor photophysics.[4,8] For many years, the interest in researching surface-induced ET has been merely fundamental. However, this effect has recently attracted interest for applications in single-molecule fluorescence microscopy[9] and fluorescence lifetime imaging.[10] The dependence between the fluorescence lifetime or intensity of an emitter and the distance from the acceptor surface has been utilized to map different biological nano-environments by localizing fluorescently labeled molecules positioned near these surfaces and converting their fluorescence lifetime values into nanometer distances.[11] Different surfaces provide a range of sensitivities at different distance ranges in the z or axial direction that extent beyond[11] or below[12] the FRET range. Monolayer graphene has enabled an 8-fold enhancement in single-molecule localization microscopy compared with gold due to its shorter dynamic range, *i.e.,* up to 40 nm compared to 150 nm in gold, and quartic distance dependency of the energy transfer efficiency, rapidly becoming a part of the single-molecule

research toolbox with applications in single-molecule biosensing, biophysics and super-resolution microscopy.[7,13–16] For instance, gold is used to probe large structures such as fixed cells[10,13] whereas graphene allows us to elucidate smaller structures, such as outer membrane protein complexes,[14] lipid bilayers,[4] and DNA dynamics.[15]

MXenes –transition metal carbides, nitrides and carbonitrides with the formula $M_{n+1}X_nT_x$– are a large family of 2D materials discovered in 2011[16] that have become prominent in the fields of energy storage,[17] sensing[18] and electromagnetic shielding.[19] However, many of their fundamental properties including nonradiative ET remain unknown, relevant for both fundamental reasons and applications in optoelectronics[20,21] and single-molecule biosensing.[15] MXenes have previously been reported to quench the fluorescence of adsorbed dyes[22–24] but a quantitative understanding of this phenomenon and its scaling with distance is lacking. To investigate this, precise nanometer-scale surface control is imperative. Our group has employed DNA nanotechnology coupled with single-molecule fluorescence microscopy to achieve the controlled placement of fluorescent dyes on surfaces.[25–29] Prior work on graphene-mediated ET using DNA origami nanopositioners resulted in experimental energy transfer quantities that lie very close to theoretical considerations.[29] We believe this is because on one hand, the addressability of the DNA origami technique allows us to control the placement of single fluorescent dyes with very high distance-precision to the surface, that of a single nucleotide (0.34 nm). On the other hand, the dye molecules are covalently attached to the phosphate backbone of DNA *via* flexible linkers, enabling free rotation of the dye molecules in solution. As a result, single emitters can adopt multiple TDM orientations in DNA origami nanopositioners,[28] important for distance calibrations, which are often modelled assuming rapidly rotating and flexible TDM orientations.[11] And finally, DNA origami structures are handled in aqueous conditions, compatible with the biological applications that many of the distance calibrations will be used for.[30]

We here describe a single-molecule fluorescence microscopy study of MXene-induced energy transfer using DNA origami nanopositioners on thin $Ti_3C_2T_x$ flakes −the most studied member of this family of 2D materials− spincast on glass coverslips. We investigate the distance dependence of the quenching phenomenon with DNA nanostructures carrying a single dye (ATTO 542) at controlled distances. In the absence of established surface immobilization chemistries for bimolecules on MXene materials, we developed a one-step method based on the known glycine-MXene interaction[31] to control the specific placement of DNA origami on MXene flakes, through triglycine-modified DNA strands.

2. Results and discussions

2.1. Thin films of $Ti_3C_2T_x$ flakes

We used $Ti_3C_2T_x$ flakes obtained by LiF-HCl exfoliation of Ti_3AlC_2 and spincast on glass coverslips (see **Methods** in **Supplementary Information)**. We obtained a discontinuous, optically transparent film (~90 % transmittance).[32] **Figure 1A** shows atomic force micrographs of the flaky films, depicting monolayer flakes that fold on themselves forming up to four-layered regions with up to 4 μm of lateral size (see height profile in Inlet; 1 layer ~1-1.5 nm). Yet, most of the large flakes range from 1 to 3 layers co-existing with smaller multilayer flakes (≤500 nm of lateral size). Supplementary Figure S1-A shows the typical UV-Vis absorption spectrum of a $Ti_3C_2T_x$ aqueous dispersion, showing the characteristic peak at ~760 nm, ascribed to plasmonic modes. The flaky films do not exhibit autofluorescence (Figure S1, inlet). Figure S2 shows a single $Ti_3C_2T_x$ flake imaged by scanning electron microscopy (SEM) and its elemental composition obtained with energy-dispersive X-ray (EDX). The X-ray diffraction (XRD) patterns of freestanding (dry) and spincast films show the typical (00l) and (002) reflections at 7.06° and 6.67°, respectively (Figure S3). The *d*-spacing was found to be 13.25 Å in the spincast films. Overall, the characterization data aligns with the typical features of $Ti_3C_2T_x$ MXene.

We performed a staining experiment of the MXene flakes with fluorescent dyes[33] to assess whether drastic differences occur in the fluorescence lifetime of the dye marked by the number of MXene layers. Single stranded DNA (ssDNA) end-labeled with ATTO 542 was used to create a fluorescent film. Figure S1 depicts the spectral overlap of the ATTO 542's emission spectrum with the absorbance spectrum of a MXene dispersion. We chose a dye that overlaps with the flat region of MXene's absorption to first investigate the nonradiative energy transfer without plasmonic coupling. Figure 1B shows a fluorescence lifetime imaging microscopy (FLIM) scan of 'stained' flakes with ATTO 542-ssDNA, where the darkest area is assumed to be the thickest MXene layers due to inner filter effects. Figure 1C shows the narrow lifetime distributions of 179 areas (0.25 μm^2) across flakes of different thicknesses – having a similar width to the unquenched dye film on glass areas. Thus, the effect of MXene thickness on $\tau_{ATTO542}$ is negligible. This lies in contrast to graphene, where the decay rate of the donor dye has been shown to scale to be proportional to the number of layers.[34,35] The thickness-independent behavior of MXenes has been previously observed for other spectroscopic properties, ascribed to their unusual weak interlayer coupling.[36–38] In our case, the short quenching dynamic range is thought to play a role, as it will be discussed later.

In the absence of routinely established bottom-up fabrication procedures for preparing large-area monolayer MXene films, we draw the following conclusions: 1) the thin films consist of large monolayer flakes that fold on themselves and predominantly form 1 to 3 layered regions in the films; 2) the effect of the 1–3-layer regime on $\tau_{ATTO542}$ is considered negligible for the following experiments.

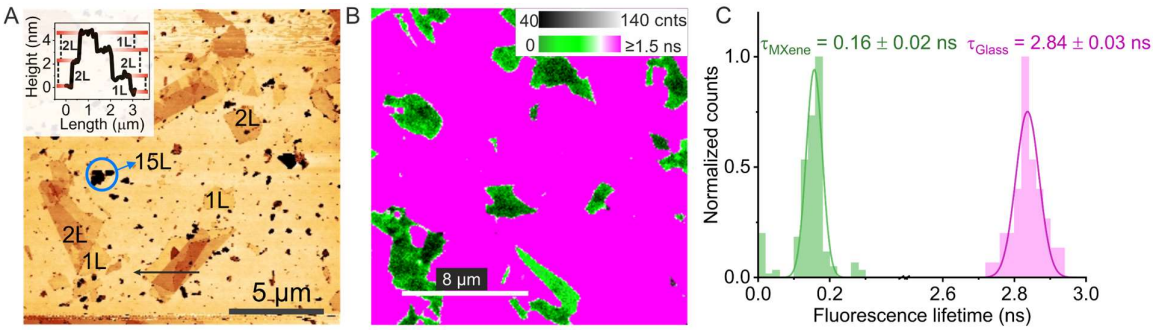

Figure 1. Flaky films: AFM characterization and FLIM assessment of MXene thickness effect on ATTO 542's fluorescence intensity and lifetime. A) Representative AFM topography of the MXene spincast films on glass (1L: one layer). Small multilayer structures are encircled. Inlet: height profile of self-folded flake. B) Representative FLIM image (20 × 20 μm, 100 nm pixel size) of flakes stained with 1 μM of ssDNA-ATTO 542 in TAE-Mg^{+2} buffer. A color-coded gradient bar is shown for fast lifetime values and a grey scale gradient for intensity values. C) Fluorescence lifetime distribution of multiple 500 × 500 nm areas (n = 179) sampled from different MXene layers and from glass areas (n = 50). Lifetime values were calculated *via* reconvolution fitting with measured IRF. The distributions were fitted using a Gaussian model. The average lifetime value and standard deviation of the distributions are displayed.

2.2. The DNA origami–MXene interface

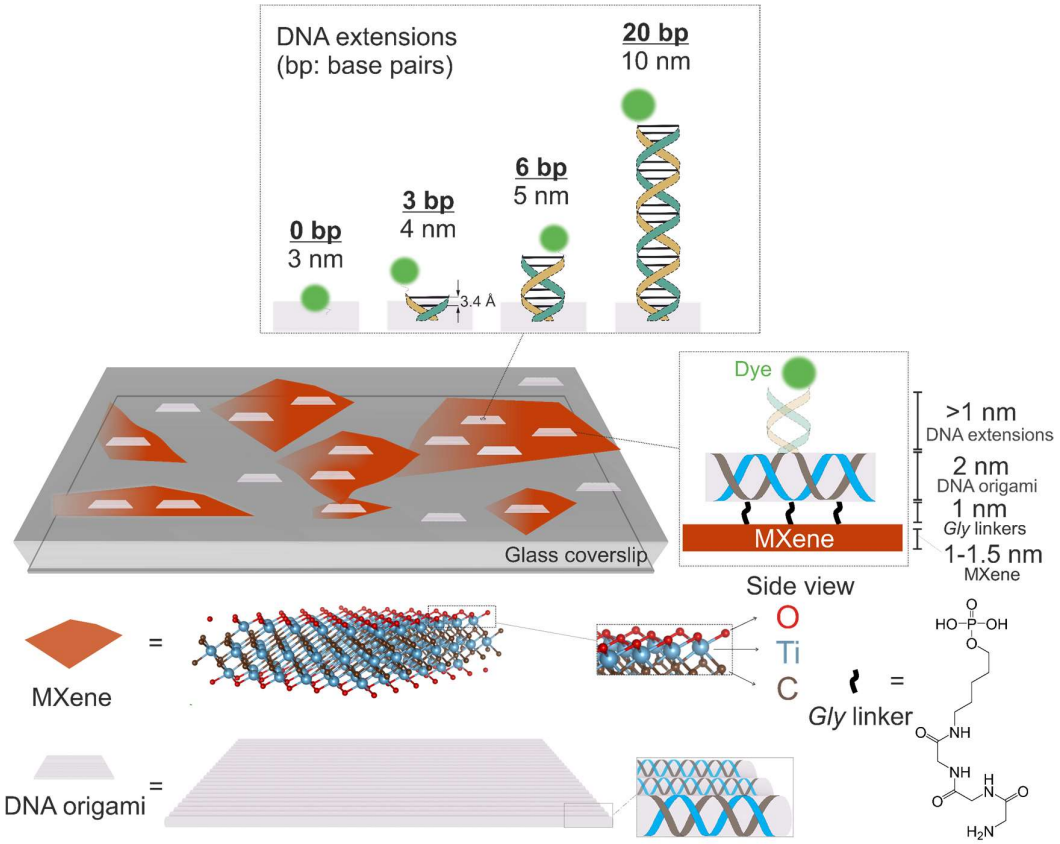

Scheme 1. DNA origami-MXene design for distance-dependent energy transfer studies at the single-molecule level. MXene flakes spincast on glass coverslips make up an optically transparent, discontinuous film with bare glass regions and flake regions. The surface groups (-O, -OH, -F) of MXenes render hydrophilic surfaces (shown in red). Rectangular DNA origami nanostructures (grey tiles) are designed to carry single donor dyes (green spheres) at different heights from the MXene surface, by modifications introduced to staple strands (grey). The long ssDNA scaffold strand is shown in blue. The contour lengths of the DNA extensions are calculated according to the number of protruding base pairs (DNA extensions, in blue and yellow). The DNA origami nanostructures are specifically immobilized *via* glycine linkers (black lines) to the surface of MXenes and non-specifically adsorbed on glass.

Scheme 1 shows a simplified representation of the system we used to probe the distance dependence of MXene-induced energy transfer. We chose a flat DNA origami nanostructure (known as new rectangular origami "NRO")[39,40] to position the dye at controlled heights from the MXene surface, anticipating an ultrashort distance sensitivity of MXenes. Figure S4 shows the caDNAno design of the NRO origami structures.

We began by establishing an immobilization chemistry to specifically anchor these nanostructures to the material surface. Inspired by the glycine-MXene chemistry previously reported in energy storage works,[31] we incorporated 6 internal staples end-labeled with commercially available triglycine moieties (referred to as *Gly* linkers in Scheme 1) in the NRO structure, together with the dye molecule facing in the opposite direction (0 bp, 3 nm, shown in Scheme 1). Glycine has been reported to bind to MXenes by forming a N–Ti covalent bond *via* glycine's primary amine.[41] The triglycine molecule was estimated to add *ca.* 1 nm spacing distance from the surface (more details in Methods). A control experiment was designed with an NRO structure without *Gly* linkers to test the specificity of the immobilization chemistry (under Mg^{2+}-free conditions). Figure S5 shows the AFM characterization of NRO nanostructures under the buffer conditions (free of divalent salts) chosen for the specific immobilization on MXene, where most of the structures appear intact. Figure 2A and B shows FLIM maps of NROs with and without *Gly*. In the glycinated system, one can see quenched dye molecules located on MXene micron-sized regions. The significantly reduced presence of NROs without *Gly* in those regions (*i.e.*, 10-fold less in a 25 μm^2 area) confirms that the immobilization on MXene takes place specifically *via Gly*. It is, however, possible to immobilize NROs without *Gly* in the presence of divalent salts (Figure S6) but they are expected to land on either side forming Mg^{2+} bridges with the phosphate backbone of dsDNA onto the MXene surface. To further explore the possible interfaces, we performed single-molecule measurements of glycinated NROs carrying down- and up-facing dyes ($NRO_{Gly\text{-}1nm}$ and $NRO_{Gly\text{-}3nm}$) and a non-glycinated dye-labeled structure ($NRO_{No\text{-}gly}$). The latter was immobilized *non-specifically* on MXene, that is, NROs anchored *via* Mg^{+2} bridges. Roughly, accounting for a ~1 nm layer of divalent ions[42] or 1 nm of *Gly* linkers at the interface and considering that the thickness of the NRO is 2 nm, we can have three distinct NRO configurations on the surface of MXenes: The dye placed at ~1 nm ($NRO_{Gly\text{-}1nm}$), 3 nm ($NRO_{Gly\text{-}3nm}$), or a mixture of the two ($NRO_{No\text{-}gly}$). Figure 2C shows the single-molecule fluorescence lifetime distributions obtained with these systems (schemes are depicted in Figure 2D) on MXene films and reference measurements with biotynilated NROs on BSA-biotin-NeutrAvidin surfaces. $NRO_{No\text{-}gly}$ showed a Gaussian distribution with both down- and up-facing subpopulations, as expected. We observed a distinction between $NRO_{Gly\text{-}1nm}$ and $NRO_{Gly\text{-}3nm}$. However, the data suggests that the dye in the $NRO_{Gly\text{-}1nm}$ is not at 1 nm from the surface. Instead, as we later came to realize through the distance dependence calibrations, the dye is on average ~2.5 ± 0.5 nm from the surface, suggesting that it predominantly displaces upwards or towards the DNA origami, as opposed to downwards or towards the surface. The

~0.5 ns shift observed from the NRO$_{Gly\text{-}1nm}$ to NRO$_{Gly\text{-}3nm}$ lifetime population thus translates only to a ~0.5 nm height difference. MXenes are therefore extremely sensitive to ultrashort distance scales.

Two possible explanations can account for the position of the dye in NRO$_{Gly\text{-}1nm}$. One is that the negatively charged dye is repelled by the MXene surface. The other is that the NRO is known to be a flexible structure where biotin-modified strands can 'tunnel' through.[43] We tested a more rigid type of DNA origami carrying a downwards-facing dye within a hexagonal lattice (nanodisc),[29] which resulted in two distinctive fluorescence lifetime populations (Figure S7) that approximately correspond to ~2.2 and 3.2 nm distances from the surface. Although we cannot explain the presence of two subpopulations, these findings confirmed that regardless of the origami structure the dye lies predominantly away from the surface. However, considering the calibration parameters obtained in the following section, the quenching measured for the NRO$_{Gly\text{-}3nm}$ system agreed with that expected from the origami design. Therefore, only systems containing fluorescent modifications on top of the DNA origami surface were considered in the distance dependence studies. Systems such as the NRO$_{Gly\text{-}1nm}$ and nanodisc origami were excluded from these investigations.

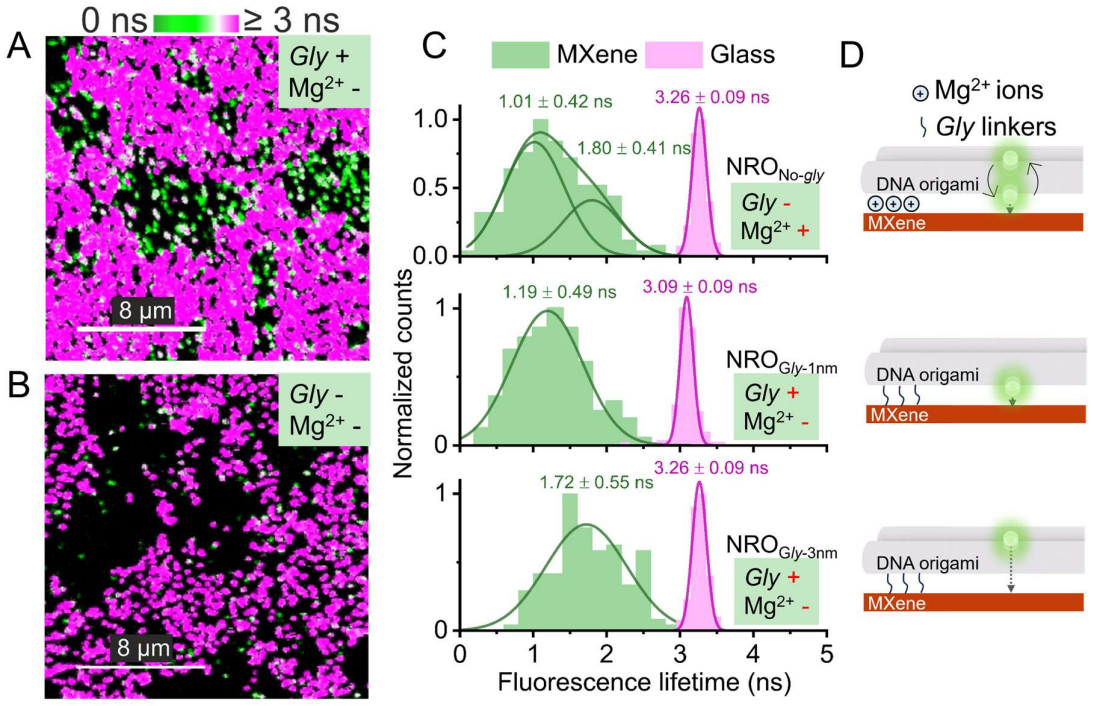

Figure 2. Specific and nonspecific immobilization of DNA origami nanostructures on MXene. FLIM scans (20 × 20 µm) of ATTO 542-labeled NRO structures on MXene films: NROs A) with and B) without *Gly* linkers in PBS-Na$^+$ buffer. A color-coded gradient bar is

shown for fast lifetime values. C) Single-molecule fluorescence lifetime histograms of different NROs and D) their schematic depictions (from top to down): without *Gly* (interacting non-specifically with the MXene surface *via* Mg^{2+} bridges in TAE-Mg^{2+} buffer); and with *Gly* carrying downwards- and upwards-facing dyes under Mg^{2+}-free conditions. The distributions were fitted using a Gaussian model. The average lifetime value and standard deviation of the distributions are displayed.

2.3. Distance dependence of MXene-induced energy transfer

Having established an immobilization protocol and having understood the DNA origami-MXene interface, we designed four NRO nanopositioners granting a range of heights to the dye from the MXene surface (Scheme 1). The 3 nm distance was designed as previously described for the $NRO_{Gly\text{-}3nm}$. Double-stranded DNA extensions were incorporated upwards to place the dye further away from the surface. The caDNAno designs are shown in Figure S4. To determine the average orientation of dsDNA protruding from the NRO, we measured the height of the donor dye with a monolayer of graphene as energy acceptor, which is a well-calibrated system in our lab. Figure S8 shows the resulting distribution and FLIM images, suggesting that a dye protruding at a contour length of 10 nm has an effective distance of 8 nm, corresponding to an averaged tilt angle of 40°.

Figure 3A shows the distributions of the fluorescence lifetime values derived from single-molecule confocal microscopy measurements of the different NROs with 3, 4, 5, and 8 nm distance to the surface (schemes in Figure 3B). The 3 nm lifetime distributions are the same data as shown in Figure 2C (bottom graph), repeated for convenience. Representative FLIM images (Figure 3C) and single-molecule intensity trajectories (Figure 3D) are also shown. Reference measurements performed on BSA-biotin-NeutrAvidin-coated glass with biotinylated NROs were performed to extract the dyes' reference lifetime values under undisturbed conditions.

Figure 3A shows the distributions of the fluorescence lifetime values derived from single-molecule confocal microscopy measurements of the different NROs. The 3 nm lifetime distributions are the same data as shown in Figure 2C (bottom graph), repeated for convenience. Representative FLIM images (Figure 3B) and single-molecule intensity trajectories (Figure 3C) are also shown. Reference measurements performed on BSA-biotin-NeutrAvidin-coated glass with biotinylated NROs were performed to extract the dyes' reference lifetime values under undisturbed conditions.

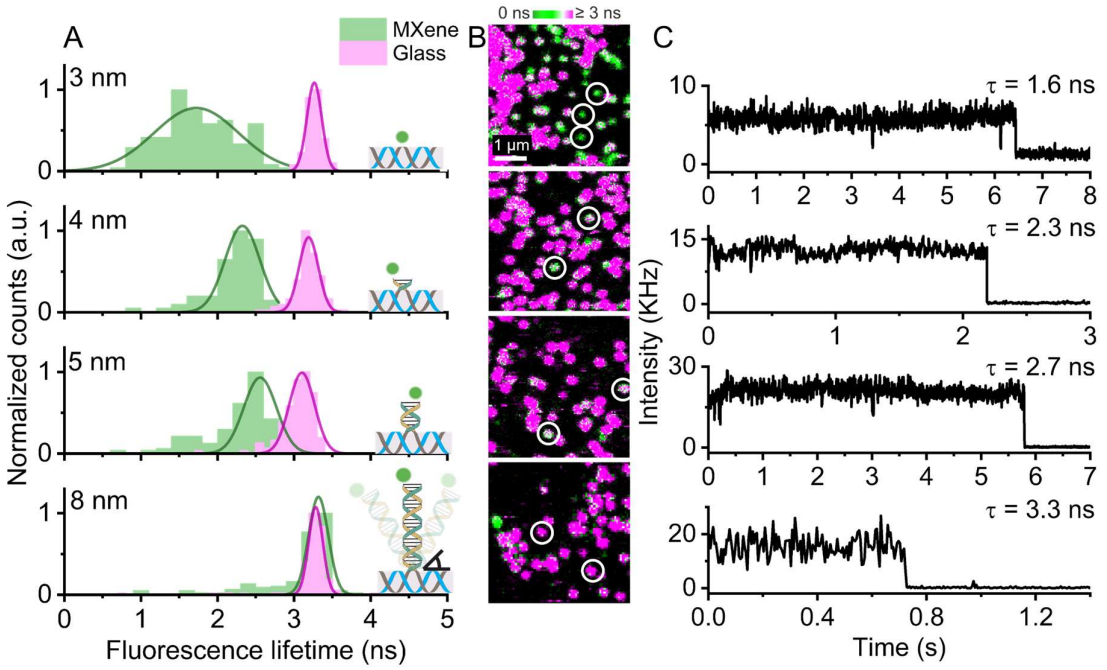

Figure 3. Single-molecule derived data from ATTO542 dyes placed at different heights from MXene substrate through DNA origami nanopositioners. A) Lifetime distributions of $n \approx 150$ molecules and the respective schemes of the NRO nanopositioners used to probe distances between 3 and 8 nm to the MXene surface. The distributions were fitted using a Gaussian model. B) Representative FLIM scans (4.5 × 4.5 µm) for each NRO with color-coded fast lifetime values of molecules on MXene (varying colors) and glass (magenta spots). White circles are used to indicate correctly oriented NROs on MXenes. C) Representative single-molecule intensity trajectories and fluorescence lifetime values of ATTO542 for each origami.

The histograms show a clear lifetime shift as the dye-MXene distance increases. The unquenched state is reached at *ca.* 8 nm, approximating the reference $\tau_{ATTO542}$ value of 3.3 ± 0.1 ns. The width of the distributions gradually decreases as the distance from MXene increases, being the highest at 3 nm (1.72 ± 0.55 ns, mean and SD), followed by 2.33 ± 0.37 ns, 2.56 ± 0.19 ns, and 3.31 ± 0.13 ns, for 4, 5 and 8 nm distances, respectively. The data dispersion at the d_0 value is an unavoidable outcome of the system as the function of the energy transfer rate shows the steepest gradient in this region.

For the 4 and 5 nm distances, the $\tau_{ATTO542}$ values of NROs on MXene were challenging to differentiate from glass adsorbed NROs at the point of data collection (see FLIM images in Figure 3B). In order to simplify the analysis, the glass-contributing regions were subtracted from the data (see Figure S9 for raw, untreated data). For the 8 nm distance, the color-coded

lifetimes of the dyes on MXene and glass could not be distinguished from each other during the measurements. Thus, the molecules were randomly selected, based on the lower density of NROs immobilized on MXene than that of glass.

Intensity traces in Figure 3C illustrating one-step photobleaching are indicative of single molecules, showing that the analysis of fluorescence lifetimes for distances between 3 and 8 nm was carried out at the single-molecule level. The lifetime values do not scale proportionally with the recorded intensity values due to the heterogeneous light absorption of the different MXene layers, and other factors such as defocusing and sample drift effects. Thus, we calculated the energy transfer efficiency (ET) only from fluorescence lifetimes as it is inversely proportional to the sum of all depopulating rate constants of the excited state and is therefore not affected by inner filter effects or sample drift. We plotted the normalized lifetime, $\frac{\tau}{\tau_0}$, and the resulting ET efficiency values against the distance from MXene surface in Figure 4A and B, respectively, where τ is the fluorescence lifetime of ATTO 542 dyes on MXene flakes and τ_0 is the fluorescence lifetime of the dyes on BSA-biotin-NeutrAvidin-functionalized glass. An exception was made for the 1 nm distance. The lifetime values for this distance were taken from the ensemble experiments shown in Figure 1. We assumed that ssDNA-ATTO542 is separated from the MXene surface by a cation layer adding an estimated height of 1 nm, according to prior molecular dynamic simulations on ssDNA-FAM adsorbed on MXene *via* salt bridges.[23] The τ_0 values were extracted from the dyes adsorbed on glass. ET efficiencies were calculated from $1 - \frac{\tau}{\tau_0}$, and the distance dependence of ET was fitted with $y = \frac{1}{\left(1+\left(\frac{x}{d_0}\right)^a\right)}$, where d_0 is the characteristic energy transfer distance (ET = 50 %) and a is the distance dependent scaling power. The fit resulted in a d_0 value of ~ 2.71 nm (± 0.16) and a distance dependency of d^{-3} (a = 2.84 ± 0.18). The latter can be understood with the following geometrical considerations: A d^{-6} dependency is ascribed to point dipole-to-dipole coupling (FRET), a d^{-4} dependency is indicative of a point dipole-to-plane coupling (*e.g.*, graphene energy transfer), and a d^{-3} dependency occurs in the case of a point dipole-to-cube coupling. The assumption of quartic distance-scaling law leads to a fit that does not follow the experimental trend, as shown in dashed lines in Figure 4B, while assuming a cubic scaling law allows achieving a proper fit of the experimental data, as depicted in dotted lines (Figure 4B). The cubic dependency reveals that the nonradiative energy transfer from an emitter to the MXene substrate is a bulk process, agreeing with prior works on transparent conductors at short distances.[12,44]

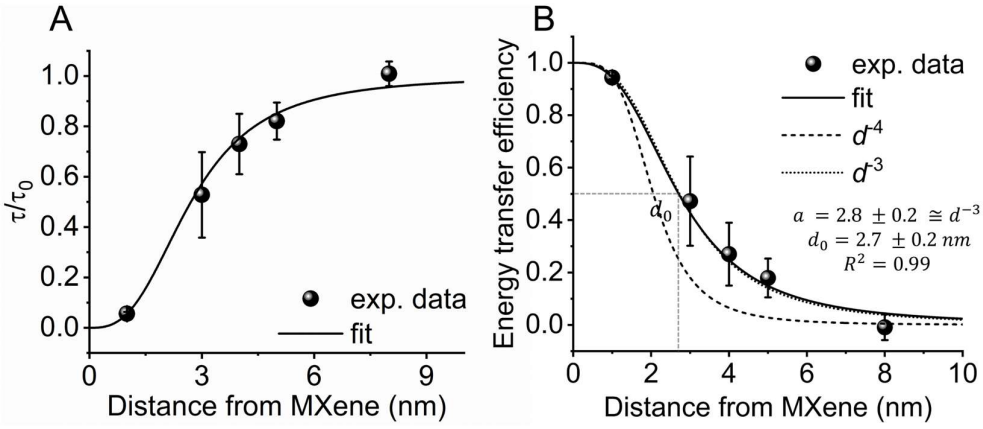

Figure 4. Distance dependence of MXene-induced energy transfer: A) Normalized lifetime as a function of distance between ATTO542 and the MXene substrate. B) Energy transfer efficiency calculated from fluorescence lifetime values as a function of the distance between ATTO542 and MXene. Fitted curve of the energy transfer efficiency as the function of the distance d between MXene and emitter ($R^2 = 0.996$), where d_0 states the distance of 50% quenching efficiency, and from the fit equals 2.71 ± 0.16 nm. The parameter a stands for the power of distance dependency, which from the fit equals 2.84 ± 0.17. Standard deviation values in both plots were calculated using error propagation from τ/τ_0 quantities. Values of τ/τ_0 and $ET_{efficiency}$ for 1 nm distance were calculated from ssDNA-ATTO542 fluorescent films (ensemble experiments) and for 3 to 8 nm from DNA origami nanopositioners (single-molecule level). Fitted curves for cubic (d^{-3}, dotted line) and quartic scaling laws (d^{-4}, dashed line) for bulk and surface processes, respectively, demonstrate adherence to d^{-3}.

We previously observed that the thickness-dependent quenching efficiency of MXenes (Figure 1) is notably less pronounced than in materials like graphene, where a second layer doubles the energy transfer rate.[34] This is because of the short quenching dynamic range of MXenes, where the d_0 value is 2.7 nm and the material's d-spacing value is 1.3 nm. In a two-layer system, with the ATTO 542 dye placed 1 nm away from the surface, an additional increase of 5% in the ET efficiency would be expected if the quenching effect were additive. This negligible effect is further supported by the fluorescence data shown in Figure 1C, where a single lifetime population centered at 0.16 ± 0.02 ns was obtained upon sampling areas with different thicknesses in the MXene films.

2.4. Final remarks

The efficacy of fluorescence quenching and its distance dependency exhibit considerable variation across different materials. This versatility has been increasingly exploited by the

fluorescence community in recent years. However, each system comes with its own set of advantages and disadvantages. For instance, ITO can reduce the fluorescence lifetime of emitters in a range of 1 to 10 nm,[12] which came as an attractive approach for the single-molecule fluorescence community looking to shrink the working range of metal-induced energy transfer (~20 -100 nm) for the study of ultrasmall biosystems. However, ITO is not commonly used as a spectroscopic ruler because of irreproducibility issues. Meanwhile graphene has found its way as a robust substrate due to its simplicity as a monolayer of a semimetal with a dynamic quenching range within ~8-25 nm, a range that has found many elegant applications in single-molecule fluorescence-based biosensing. Yet, graphene's surface properties –hydrophobic, strong effect of multilayered regions on lifetime and defects adding abrupt hydrophilic regions in the hydrophobic lattice– can be challenging to work with when assembling and studying complex systems such as lipid bilayers and protein complexes. $Ti_3C_2T_x$ MXene surprisingly has a quenching capability comparable to that of ITO despite not being as transparent. This material can be a promising alternative to graphene and metals for applications in which the desired working range is below 10 nm and the substrate is required to be hydrophilic. Moreover, MXene is a robust material in that variabilities arising from thickness are believed to be less impactful than with other substrates. However, more efforts in engineering stable monolayer films are needed to make use of their extraordinary sensitivity at ultrashort distances for single-molecule biosensing applications.

3. Conclusions

We presented for the first time the distance dependency of MXene-induced nonradiative energy transfer. Utilizing glycine-modified DNA oligonucleotides, we specifically immobilized DNA origami structures on MXene substrates. This method enabled the specific placement of fluorescent dyes onto MXene flakes at controlled heights. Our single-molecule fluorescence lifetime results showed a d^{-3} dependence of the energy transfer from a green dye to MXene. The 50% energy transfer distance (d_0) was determined to be 2.7 ± 0.2 nm, highlighting the strength of coupling interactions at close distances.

MXene's inherent transparency and distance dependent fluorescence quenching position it as a promising nanoruler substrate for single-molecule microscopy applications. Especially when there is a need for high z-detection sensitivity at ultra-short distance regimes using a hydrophilic substrate. Other areas such as nanophotonics and optoelectronics may also benefit from the integration of DNA origami and MXene to accurate place molecules of interest at controlled dimensions. Moreover, the substitution of graphene anodes with MXene anodes in

solar cells could be advantageous given that MXene has a d_0 value that is six times smaller than that of graphene. This would lead to reduced exciton quenching in the active layer, thereby enhancing charge separation yield.

Our study contributes to the integration of 2D materials with single-molecule fluorescence microscopy. As the field is still in early stages, we recognize the potential in examining other low-dimensional, metal-like materials, particularly those that are hydrophilic and biocompatible to make the most out of this emerging area of research.[45] We aim to deepen our understanding of the MXene family of materials in this context, addressing aspects like surface and bulk effects, prevalent plasmonic modes, and develop strategies to achieve uniform film quality.

Supporting Information

Supporting Information is available.

Acknowledgements

The authors thank for financial support by the Deutsche Forschungsgemeinschaft (DFG, German Research Foundation) under grant numbers TI 329/14-1 and KA 5449/2-1, the excellence cluster e-conversion under Germany's Excellence Strategy – EXC 2089/1 – 390776260, and by the Center for NanoScience (CeNS). Furthermore, funded by the Federal Ministry of Education and Research (BMBF) and the Free State of Bavaria under the Excellence Strategy of the Federal Government and the Länder through the ONE MUNICH Project Munich Multiscale Biofabrication. C.L.M.-P. and A.M.S. are thankful for the support by the Alexander von Humboldt foundation under references Ref. 3.3 – ESP – 1218808 – HFST-P, and Ref. 3.2 – ARG – 1220722 – GF-P.

References

[1] K. H. Drexhage, *Journal of Luminescence* **1970**, *1–2*, 693.

[2] R. R. Chance, A. H. Miller, A. Prock, R. Silbey, *The Journal of Chemical Physics* **1975**, *63*, 1589.

[3] T. Förster, *Zeitschrift für Naturforschung B* **1947**, *2*, 174.

[4] T. Chen, A. Ghosh, J. Enderlein, *Nano Lett.* **2023**, *23*, 2421.

[5] G. Agam, C. Gebhardt, M. Popara, R. Mächtel, J. Folz, B. Ambrose, N. Chamachi, S. Y. Chung, T. D. Craggs, M. de Boer, D. Grohmann, T. Ha, A. Hartmann, J. Hendrix, V. Hirschfeld, C. G. Hübner, T. Hugel, D. Kammerer, H.-S. Kang, A. N. Kapanidis, G.

Krainer, K. Kramm, E. A. Lemke, E. Lerner, E. Margeat, K. Martens, J. Michaelis, J. Mitra, G. G. Moya Muñoz, R. B. Quast, N. C. Robb, M. Sattler, M. Schlierf, J. Schneider, T. Schröder, A. Sefer, P. S. Tan, J. Thurn, P. Tinnefeld, J. van Noort, S. Weiss, N. Wendler, N. Zijlstra, A. Barth, C. A. M. Seidel, D. C. Lamb, T. Cordes, *Nat Methods* **2023**, *20*, 523.

[6] B. Hellenkamp, S. Schmid, O. Doroshenko, O. Opanasyuk, R. Kühnemuth, S. Rezaei Adariani, B. Ambrose, M. Aznauryan, A. Barth, V. Birkedal, M. E. Bowen, H. Chen, T. Cordes, T. Eilert, C. Fijen, C. Gebhardt, M. Götz, G. Gouridis, E. Gratton, T. Ha, P. Hao, C. A. Hanke, A. Hartmann, J. Hendrix, L. L. Hildebrandt, V. Hirschfeld, J. Hohlbein, B. Hua, C. G. Hübner, E. Kallis, A. N. Kapanidis, J.-Y. Kim, G. Krainer, D. C. Lamb, N. K. Lee, E. A. Lemke, B. Levesque, M. Levitus, J. J. McCann, N. Naredi-Rainer, D. Nettels, T. Ngo, R. Qiu, N. C. Robb, C. Röcker, H. Sanabria, M. Schlierf, T. Schröder, B. Schuler, H. Seidel, L. Streit, J. Thurn, P. Tinnefeld, S. Tyagi, N. Vandenberk, A. M. Vera, K. R. Weninger, B. Wünsch, I. S. Yanez-Orozco, J. Michaelis, C. A. M. Seidel, T. D. Craggs, T. Hugel, *Nat Methods* **2018**, *15*, 669.

[7] W. R. Algar, N. Hildebrandt, S. S. Vogel, I. L. Medintz, *Nat Methods* **2019**, *16*, 815.

[8] H. S. Chung, J. M. Louis, W. A. Eaton, *Biophysical Journal* **2010**, *98*, 696.

[9] N. Karedla, A. I. Chizhik, I. Gregor, A. M. Chizhik, O. Schulz, J. Enderlein, *ChemPhysChem* **2014**, *15*, 705.

[10] A. I. Chizhik, J. Rother, I. Gregor, A. Janshoff, J. Enderlein, *Nature Photon* **2014**, *8*, 124.

[11] A. Ghosh, A. I. Chizhik, N. Karedla, J. Enderlein, *Nat Protoc* **2021**, *16*, 3695.

[12] R. J. Moerland, J. P. Hoogenboom, *Optica* **2016**, *3*, 112.

[13] L. Hauke, S. Isbaner, A. Ghosh, I. Guido, L. Turco, A. I. Chizhik, I. Gregor, N. Karedla, F. Rehfeldt, J. Enderlein, *ACS Nano* **2023**, *17*, 8242.

[14] N. Füllbrunn, Z. Li, L. Jorde, C. P. Richter, R. Kurre, L. Langemeyer, C. Yu, C. Meyer, J. Enderlein, C. Ungermann, J. Piehler, C. You, *eLife* **2021**, *10*, e62501.

[15] I. Kamińska, J. Bohlen, R. Yaadav, P. Schüler, M. Raab, T. Schröder, J. Zähringer, K. Zielonka, S. Krause, P. Tinnefeld, *Advanced Materials* **2021**, *33*, 2101099.

[16] M. Naguib, M. Kurtoglu, V. Presser, J. Lu, J. Niu, M. Heon, L. Hultman, Y. Gogotsi, M. W. Barsoum, *Advanced Materials* **2011**, *23*, 4248.

[17] B. Anasori, M. R. Lukatskaya, Y. Gogotsi, *Nat Rev Mater* **2017**, *2*, 1.

[18] B. Xu, M. Zhu, W. Zhang, X. Zhen, Z. Pei, Q. Xue, C. Zhi, P. Shi, *Advanced Materials* **2016**, *28*, 3333.

[19] F. Shahzad, M. Alhabeb, C. B. Hatter, B. Anasori, S. Man Hong, C. M. Koo, Y. Gogotsi, *Science* **2016**, *353*, 1137.

[20] Z. Liu, H. N. Alshareef, *Advanced Electronic Materials* **2021**, *7*, 2100295.

[21] S. Panuganti, L. V. Besteiro, E. S. Vasileiadou, J. M. Hoffman, A. O. Govorov, S. K. Gray, M. G. Kanatzidis, R. D. Schaller, *J. Am. Chem. Soc.* **2021**, *143*, 4244.

[22] Q. Zhang, F. Wang, H. Zhang, Y. Zhang, M. Liu, Y. Liu, *Anal. Chem.* **2018**, *90*, 12737.

[23] C. L. Manzanares-Palenzuela, A. M. Pourrahimi, J. Gonzalez-Julian, Z. Sofer, M. Pykal, M. Otyepka, M. Pumera, *Chem. Sci.* **2019**, *10*, 10010.

[24] Z. Huang, B. Liu, J. Liu, *Langmuir* **2019**, *35*, 9858.

[25] S. Isbaner, N. Karedla, I. Kaminska, D. Ruhlandt, M. Raab, J. Bohlen, A. Chizhik, I. Gregor, P. Tinnefeld, J. Enderlein, R. Tsukanov, *Nano Lett.* **2018**, *18*, 2616.

[26] G. P. Acuna, M. Bucher, I. H. Stein, C. Steinhauer, A. Kuzyk, P. Holzmeister, R. Schreiber, A. Moroz, F. D. Stefani, T. Liedl, F. C. Simmel, P. Tinnefeld, *ACS Nano* **2012**, *6*, 3189.

[27] C. Steinhauer, R. Jungmann, T. L. Sobey, F. C. Simmel, P. Tinnefeld, *Angewandte Chemie International Edition* **2009**, *48*, 8870.

[28] I. H. Stein, V. Schüller, P. Böhm, P. Tinnefeld, T. Liedl, *ChemPhysChem* **2011**, *12*, 689.

[29] I. Kaminska, J. Bohlen, S. Rocchetti, F. Selbach, G. P. Acuna, P. Tinnefeld, *Nano Lett.* **2019**, *19*, 4257.

[30] M. Scheckenbach, J. Bauer, J. Zähringer, F. Selbach, P. Tinnefeld, *APL Materials* **2020**, *8*, 110902.

[31] C. Chen, M. Boota, P. Urbankowski, B. Anasori, L. Miao, J. Jiang, Y. Gogotsi, *J. Mater. Chem. A* **2018**, *6*, 4617.

[32] C. (John) Zhang, B. Anasori, A. Seral-Ascaso, S.-H. Park, N. McEvoy, A. Shmeliov, G. S. Duesberg, J. N. Coleman, Y. Gogotsi, V. Nicolosi, *Advanced Materials* **2017**, *29*, 1702678.

[33] J. Kim, L. J. Cote, F. Kim, J. Huang, *J. Am. Chem. Soc.* **2010**, *132*, 260.

[34] A. Raja, A. Montoya−Castillo, J. Zultak, X.-X. Zhang, Z. Ye, C. Roquelet, D. A. Chenet, A. M. van der Zande, P. Huang, S. Jockusch, J. Hone, D. R. Reichman, L. E. Brus, T. F. Heinz, *Nano Lett.* **2016**, *16*, 2328.

[35] Z. Chen, S. Berciaud, C. Nuckolls, T. F. Heinz, L. E. Brus, *ACS Nano* **2010**, *4*, 2964.

[36] J. K. El-Demellawi, S. Lopatin, J. Yin, O. F. Mohammed, H. N. Alshareef, *ACS Nano* **2018**, *12*, 8485.

[37] H. Kim, M. I. Nugraha, X. Guan, Z. Wang, M. K. Hota, X. Xu, T. Wu, D. Baran, T. D. Anthopoulos, H. N. Alshareef, *ACS Nano* **2021**, *15*, 5221.

[38] V. Mauchamp, M. Bugnet, E. P. Bellido, G. A. Botton, P. Moreau, D. Magne, M. Naguib, T. Cabioc'h, M. W. Barsoum, *Phys. Rev. B* **2014**, *89*, 235428.

[39] J. J. Schmied, M. Raab, C. Forthmann, E. Pibiri, B. Wünsch, T. Dammeyer, P. Tinnefeld, *Nat Protoc* **2014**, *9*, 1367.

[40] N. V. Voigt, T. Tørring, A. Rotaru, M. F. Jacobsen, J. B. Ravnsbæk, R. Subramani, W. Mamdouh, J. Kjems, A. Mokhir, F. Besenbacher, K. V. Gothelf, *Nature Nanotech* **2010**, *5*, 200.

[41] J. D. Gouveia, G. Novell-Leruth, P. M. L. S. Reis, F. Viñes, F. Illas, J. R. B. Gomes, *ACS Appl. Bio Mater.* **2020**, *3*, 5913.

[42] B. E. Conway, *Ionic Hydration in Chemistry and Biophysics*, Elsevier Scientific Publishing Company, **1981**.

[43] R. Jungmann, M. S. Avendaño, J. B. Woehrstein, M. Dai, W. M. Shih, P. Yin, *Nat Methods* **2014**, *11*, 313.

[44] W. L. Barnes, *Journal of Modern Optics* **1998**, *45*, 661.

[45] L. Richter, A. M. Szalai, C. L. Manzanares-Palenzuela, I. Kamińska, P. Tinnefeld, *Advanced Materials* **2023**, *35*, 2303152.